

Clump mass function at an early stage of molecular cloud evolution: II. Galactic cloud complexes

Todor V. Veltchev^{1,2*}, Sava Donkov³, and Ralf S. Klessen²

¹ *University of Sofia, Faculty of Physics, 5 James Bourchier Blvd., 1164 Sofia, Bulgaria*

² *Universität Heidelberg, Zentrum für Astronomie, Institut für Theoretische Astrophysik, Albert-Überle-Str. 2, 69120 Heidelberg, Germany*

³ *Department of Applied Physics, Technical University, 8 Kliment Ohridski Blvd., 1000 Sofia, Bulgaria*

Accepted 2013, April 22

ABSTRACT

The statistical approach for derivation of the clump mass function (ClMF) developed by Donkov, Veltchev & Klessen is put to observational test through comparison with mass distributions of clumps from molecular emission and dust continuum maps of Galactic cloud complexes, obtained by various authors. The results indicate gravitational boundedness of the dominant clump population, with or without taking into account the contribution of their thermal and magnetic energy. The ClMF can be presented by combination of two power-law functions separated by a characteristic mass from about ten to hundreds solar masses. The slope of the intermediate-mass ClMF is shallow and nearly constant ($-0.25 \gtrsim \Gamma_{\text{IM}} \gtrsim -0.55$) while the high-mass part is fitted by models that imply gravitationally unstable clumps and exhibit slopes in a broader range ($-0.9 \gtrsim \Gamma_{\text{IM}} \gtrsim -1.6$), centered at the value of the stellar initial mass function ($\Gamma_{\text{HM}} \gtrsim -1.3$).

Key words: ISM: clouds - ISM: structure - turbulence - methods: statistical

1 INTRODUCTION

Dense clumps in molecular clouds (MCs) are typical sites of star formation as they are often associated with young stellar objects. Their origin can be sought in the early epoch of cloud evolution when supersonic turbulence creates sets of condensations in the cold, mainly molecular gas. Recent numerical simulations indicate their mean densities, sizes and masses vary in ranges $10^2 - 10^4 \text{ cm}^{-3}$, $0.04 - 1 \text{ pc}$ and $0.1 - 10^3 M_{\odot}$, respectively (Vázquez-Semadeni et al. 2007; Banerjee et al. 2009; Shetty et al. 2010), in consistency with extensive observational data about MC clumps (e.g., Bergin & Tafalla 2007). Clump morphology is also diverse: from filamentary to compact, quasi-spherical shapes (Hennebelle et al. 2008). Gravitational stability analysis shows that some clumps are subject to further contraction and collapse and eventually give birth to single stars or stellar clusters.

Numerous individual clumps were initially identified on maps of molecular line emissions which trace different density regimes in MCs: ^{12}CO ($n \sim 10^2 \text{ cm}^{-3}$), ^{13}CO and C^{18}O ($n \sim 10^3 \text{ cm}^{-3}$), CS ($J = 1 - 0$) and H^{13}CO^+ ($J = 1 - 0$) ($n \gtrsim 10^4 \text{ cm}^{-3}$). Such surveys were performed in nearby (at distances $< 500 \text{ pc}$) Galactic cloud complexes like Orion A (Tatematsu et al. 1993),

Orion B (Kramer et al. 1998), Taurus (Onishi et al. 1996), Ophiuchus (Tachihara et al. 2000), Lupus (Hara et al. 1999) and many others. Some of these results on the physical parameters of clumps were included in the statistical study of Tachihara et al. (2002) who considered a sample of 9 Galactic star-forming regions. In the last decade, further intensive research of MCs by use of some high-density tracers like H^{13}CO^+ ($J = 1 - 0$) (Onishi et al. 2002; Ikeda, Sunada & Kitamura 2007; Ikeda, Kitamura & Sunada 2009) as well of dust continuum (Johnstone et al. 2001; Kerton et al. 2001; Johnstone, Matthews & Mitchell 2006; Reid & Wilson 2005, 2006a; Di Francesco et al. 2010) and dust extinction (e.g. Alves, Lombardi & Lada 2007) observations allowed for more precise mapping of cloud structure. Some clumps originally found on emission maps were further decomposed and more compact (typical sizes $\lesssim 0.2 \text{ pc}$), very dense ($n \gtrsim 10^5 \text{ cm}^{-3}$) and probably collapsing clumps were delineated. Some authors call such objects ‘dense cores’; hereafter, we label them simply *cores*.

It is suggested that cores eventually form stars (Bergin & Tafalla 2007) and thus the study of their mass function (CMF) will enable a better understanding of the physical origin of the stellar initial mass function (IMF) and its possible variations. Indeed, numerous dust continuum and dust extinction observations demonstrate that the CMF resembles the IMF in its shape when fitted by a single

* E-mail: eirene@phys.uni-sofia.bg

power-law (Testi & Sargent 1998; Johnstone et al. 2001), a combination of two power-law (Motte, André & Neri 1998; Motte & André 2001; Johnstone, Matthews & Mitchell 2006; Nutter & Ward-Thompson 2007) or a lognormal function (Stanke et al. 2006; Enoch et al. 2008; Könyves et al. 2010). It therefore has been proposed that the IMF is a direct product of the CMF and a uniform star formation efficiency (Alves, Lombardi & Lada 2007).

Yet it is still unclear how the CMF originates from the mass distribution of the initially formed MC clumps. The clump mass function (CIMF), as derived from molecular line emission surveys of Galactic star-forming regions using low- and moderate-density tracers, varies in shape and slope and often differs substantially from the IMF. Most of the earlier studies of nearby complexes from CO mapping resulted in a single power-law CIMF of a rather shallow slope $-0.3 \gtrsim \Gamma \gtrsim -0.8$ without any characteristic mass M_{ch} (Stutzki & Güsten 1990; Blitz 1993; Williams, Blitz & Stark 1995; Heithausen et al. 1998) – in contrast to the Salpeter slope -1.3 (Salpeter 1955) of the high-mass IMF over $M_{\text{ch}} \sim 0.5 M_{\odot}$. Moreover, the CIMF slope Γ was found to remain nearly constant for a large range of clump masses $10^{-3} \leq m/M_{\odot} \leq 10^4$, in different MCs (Kramer et al. 1998).

Later works allowed for a more detailed mapping of MCs. Emission from CO molecules was found to trace lower density cloud regions. Tracers like C^{18}O revealed structures with $n \sim 10^4 \text{ cm}^{-3}$ but essentially larger ($l \sim 0.1 - 0.5 \text{ pc}$) than prestellar cores (Hara et al. 1999; Tachihara et al. 2000, 2002). Such compact clumps encompass about 10% of the cloud mass. It was demonstrated that the derived CIMFs could be represented by a combination of 2 power-law functions as $M_{\text{ch}} \sim 15 - 20 M_{\odot}$ separates intermediate-mass from high-mass CIMF, with slopes $-0.3 \gtrsim \Gamma_{\text{IM}} \gtrsim -0.7$ and $\Gamma_{\text{HM}} \lesssim -1.5$, respectively. This general picture was confirmed from submillimeter continuum studies of MC complexes at kpc-scale distances. Using $450 \mu\text{m}$ and $850 \mu\text{m}$ SCUBA maps, Reid & Wilson derived 2 power-law CIMFs for two massive star-forming regions. For NGC 7538, they obtained $M_{\text{ch}} \sim 100 M_{\odot}$ and $\Gamma_{\text{IM}} \sim 0$ while the variations of the high-mass slope seem to be more sensitive to the wavelength and close to the Salpeter value: $-1 \gtrsim \Gamma_{\text{HM}} \gtrsim -1.6$ (Reid & Wilson 2005). For M17, the characteristic mass turned out to be an order of magnitude less ($M_{\text{ch}} \sim 8 - 20 M_{\odot}$), the intermediate mass slopes are positive ($\Gamma_{\text{IM}} \sim 0.5 - 1$) and the high-mass ones are about the value for CO clumps $-0.5 \gtrsim \Gamma_{\text{HM}} \gtrsim -0.9$ (Reid & Wilson 2006a). Extending further their study to 11 low- and high-mass star-forming regions, those authors conclude that a single power-law CIMF is clearly ruled out and argue for a two power-law function with $-0.2 \gtrsim \Gamma_{\text{IM}} \gtrsim -0.7$ and Γ_{HM} about the Salpeter slope, regardless of the diversity of characteristic masses (Reid & Wilson 2006b).

The predictions of our statistical model (Donkov, Veltchev & Klessen 2012, hereafter, Paper I) are generally consistent with a two power-law CIMF with shallow intermediate-mass slope Γ_{IM} and steeper high-mass slope Γ_{HM} , allowing for a variety of M_{ch} within two orders of magnitude. In this work they are compared with results on the observational CIMF: i) from molecular-line studies of three nearby star-forming regions: Orion A (Tatematsu et al. 1993), Orion B (Kramer et al.

1998), Taurus (Onishi et al. 1996), and of a sample of 9 regions (Tachihara et al. 2002); ii) from dust continuum surveys and CO mappings of 2 kpc-away regions: M17 (Reid & Wilson 2006a; Stutzki & Güsten 1990) and Rosette (Di Francesco et al. 2010; Williams, Blitz & Stark 1995). We define *clumps* as condensations formed through a turbulent cascade during the early MC evolution. The ensemble of clumps generated at given spatial scale L obeys a power-law relationship between clump masses and densities $n \propto m^x$ where the exponent $x = x(L)$ is calculated considering equipartition relations between various forms of energy: gravitational, turbulent (kinetic), thermal (internal) and magnetic (Donkov, Veltchev & Klessen 2011, hereafter, DVK11). The CIMF is derived as a superposition of clump mass distributions over a range of scales, taking into account the fractal structure of the cloud (Paper I).

The physical basis of the model, its free parameters and the construction of the CIMF are recalled in Section 2. The clump mass distribution derived from modeled structure of each considered individual cloud as well as different distributions that fit the composite observational CIMF are presented and commented in Section 3. Section 4 contains a discussion on the applicability and the restrictions of our approach to predict the observational CIMF and envisions its possible extensions. Our conclusions are summarized in Section 5.

2 STRUCTURE AND CLUMP MASS FUNCTION OF INDIVIDUAL CLOUD

2.1 Physical framework of the model

Our statistical model for clump description is presented in details in DVK11 (Sect. 2 and 3) and Paper I (Sect. 2). Its main assumptions can be summarized as follows:

(i) *Scaling laws within the turbulent cloud:* We consider fully developed supersonic turbulence that implies homogeneous and isotropic stochastic medium with a fractal structure and well-defined scaling laws of turbulent velocity, mean density and mean magnetic field. Turbulent flows create density structures at any scale in the inertial range $L_{\text{max}} \gtrsim L \gtrsim L_{\text{min}}$ through a cascade possibly driven by the very process of cloud formation (Klessen & Hennebelle 2010). We estimate the upper limit $L_{\text{max}} = 20 \text{ pc}$ adopting a typical size of giant MC $\sim 50 \text{ pc}$ as an injection scale and taking in view that the largest scale of the turbulence inertial range is about a factor of 3 less (Kritsuk et al. 2007; Padoan et al. 2006). The lower limit L_{min} is imposed above the actual end of the inertial range from the construction of our model: the sizes l of all clumps generated at given scale L must be within the inertial range and are typically an order of magnitude less than L . Various observations show that the inertial range spans at least 3 orders of magnitude, i.e. the size of the smallest generated object l_{min} must be about 0.02 pc . We consider mainly molecular and isothermal gas with temperatures $T = 10 - 20 \text{ K}$. Requiring supersonic medium at all fractal scales and by use of a typical velocity scaling (see equation 1 below), one obtains $l_{\text{min}} \gtrsim 0.05 \text{ pc}$ which yields a scale of its generation $L_{\text{min}} \simeq 0.5 \text{ pc}$.

Turbulent velocity dispersion u and mean mass density $\langle \rho \rangle$ are assumed to scale according to “Larson’s first and second

laws” (Larson 1981) whereas the scaling relation of the mean magnetic field B is obtained from its observationally verified relation to the mean mass density ($B \propto \langle \rho \rangle^{1/2}$; Crutcher 1999):

$$u = 1.1 L^\beta \quad [\text{km s}^{-1}] , \quad (1)$$

$$\langle \rho \rangle = 13.6 \times 10^{-21} L^\alpha \quad [\text{g cm}^{-3}] , \quad (2)$$

$$B = 50 L^{0.5\alpha} \quad [\mu\text{G}] , \quad (3)$$

A fixed velocity scaling index β is chosen. While observational and numerical studies indicate a broad range $0.2 \lesssim \beta \lesssim 0.65$, the results in this Paper narrow it to $0.2 \lesssim \beta \leq 0.47$ (‘soft’ velocity scaling). The density scaling index $\alpha = \alpha(L)$ is derived self-similarly from the assumption of mass-density relationship for clumps generated at a given scale L (see below).

(ii) *Lognormal clump density distribution*: Such volumetric distribution of mass density ρ is testified from numerous numerical simulations of supersonic turbulence and is described through a standard lognormal probability density function (pdf):

$$p(s) ds = \frac{1}{\sqrt{2\pi\sigma^2}} \exp \left[-\frac{1}{2} \left(\frac{s - s_{\max}}{\sigma} \right)^2 \right] ds , \quad (4)$$

where s is the log density and (s_{\max}, σ) are the distribution peak and the standard deviation, respectively. In our model, this density statistics is used as the basis of clump statistics as follows. Let N_{tot}^p is the total number of pixels in a cloud map and N_ρ^p is the number of those with density ρ . Then

$$\frac{N_\rho^p}{N_{\text{tot}}^p} \sim \frac{1}{\sqrt{2\pi\sigma^2}} \exp \left[-\frac{1}{2} \left(\frac{s - s_{\max}}{\sigma} \right)^2 \right] .$$

Since turbulence is assumed to be homogeneous and isotropic and gravity is a central force, one can consider the generated clumps as homogeneous spheres, characterized solely by their size (diameter) l . Of course, the real fragments in a turbulent MC with high Mach numbers (≥ 3) delineated by isodensity contours $[\rho - \Delta\rho, \rho + \Delta\rho]$ can be with complex shapes and even not necessarily connected regions. The essence of our statistical approach is to describe them by an ensemble of $N_\rho^c \propto (N_\rho^p/N_{\text{tot}}^p)$ spherical homogeneous clumps with density ρ . Thus the ‘average clump ensemble’ generated at given spatial scale L follows a log-normal density distribution like the pdf at that scale.

The parameters of the density distribution:

$$\sigma^2 = \ln(1 + b^2 \mathcal{M}^2) , \quad s_{\max} = -\frac{\sigma^2}{2} \quad (5)$$

depend on the spatial scale through the sonic Mach number $\mathcal{M} = u(L)/c_s$ where c_s is the sound speed. The turbulence forcing parameter b spans values between 0.33, for purely solenoidal forcing, and 1.00, for purely compressive forcing (see Federrath et al. (2010)). The modeled CIMFs presented in this Paper favor mainly solenoidal forcing, mixed in a natural way with compressive modes: $b \leq 0.46$. A comment on that is included in the Discussion.

(iii) *Clump mass-density-size relationship*: Masses, densities and sizes of clumps in an ‘average ensemble’ are assumed to obey the statistical relationships:

$$\ln \left(\frac{\rho}{\rho_0} \right) = x \ln \left(\frac{m}{m_0} \right) \quad (6)$$

$$\ln \left(\frac{\rho}{\rho_0} \right) = \frac{3x}{1-x} \ln \left(\frac{l}{l_0} \right) , \quad (7)$$

with a choice of normalization units:

$$\rho_0 \equiv \langle \rho \rangle \quad (8)$$

$$l_0 \equiv \kappa L \quad (9)$$

$$\frac{\rho_0 l_0^3}{m_0} \propto \exp \left(\sigma^2 \times \frac{1-x}{x} \right) \quad (10)$$

The dimensionless parameter κ accounts for the precision of the clump size ‘measurement’ and can be interpreted as mapping resolution of the scale of clump generation. It is appropriate to set it as a small constant of order of several percent since l is typically an order of magnitude less than L .

According to our turbulent scenario of clump formation, the clump density-size relationship (equation 7) is taken as a self-similar extension of the density scaling law (equation 2) and hence:

$$\alpha = \frac{3x}{1-x} . \quad (11)$$

(iv) *Equipartitions between clump energies*: A general type of equipartition relation between gravitational W and kinetic E_{kin} energy per unit volume with some coefficient f_{gk} of proportionality

$$|W| \sim f_{\text{gk}} E_{\text{kin}} ,$$

is expected to hold for structures shaped by turbulence in which gravity gradually takes over; e.g. in regions where turbulence decays locally or where it accumulates material reaching a state of local gravitational instability. A fiducial range $1 \leq f_{\text{gk}} \leq 4$ is testified from simulations of the early stage of the clump evolution, before stars have been formed (Vázquez-Semadeni et al. 2007). The analysis of MHD simulations of cloud formation at Galactic scale (length unit ~ 1 kpc; Passot et al. 1995) showed that the considered equipartition can include contributions of thermal (internal) E_{th} and magnetic E_{mag} energy as well (Ballesteros-Paredes & Vázquez-Semadeni 1995).

In our model, we assume such equipartition relations to hold for the ‘average clump ensemble’ and use them to derive the mass-density scaling index $x(L)$ at each scale:

- **wkin2** or **wkin4**, equipartition of the gravitational vs. kinetic energy:

$$|W| \sim 2E_{\text{kin}} , \quad (12)$$

$$|W| \sim 4E_{\text{kin}} . \quad (13)$$

- **wkin2mag**, equipartition of the gravitational vs. kinetic and magnetic energy:

$$|W| \sim 2E_{\text{kin}} + E_{\text{mag}} . \quad (14)$$

- **wkin2th2**, equipartition of the gravitational vs. kinetic and thermal energy:

$$|W| \sim 2E_{\text{kin}} + 2E_{\text{th}} . \quad (15)$$

The corresponding equations for the typical member of the ‘average clump ensemble’ which are used to derive $x(L)$ are listed in Paper I (Appendix A and B).

2.2 Free parameters of the model and cloud structure from extinction maps

In our model, a MC is considered as a hierarchical set of spatial scales and its structure is described through the solutions $x(L)$ obtained for a chosen equipartition relation. They depend on four free parameters: velocity-scaling index β , turbulent forcing parameter b , mapping resolution κ (equation 9) and temperature T . The parameters' ranges of variation that yield plausible solutions can be restricted by use of observational studies of MC structure. The work of Lombardi, Alves & Lada (2010, hereafter, LAL10), based on dust extinction maps of Galactic cloud complexes, corresponds best to our approach. These authors define an 'effective radius $R_s = \sqrt{S/\pi}$ of a subregion or a set of subregions with total area S which we interpret as an observational counterpart of our notion of 'spatial scale', i.e. $L = 2R_s$. Then the MC structure is described by the relationship between the effective radius and the mass within the total area S : $M_s \propto R_s^\gamma$ (see Fig. 2 in LAL10). On the other hand, the total mass contained within a scale L depends, in our approach, on the index $x(L)$ due to the self-similarity assumption (cf. equations 7 and 11): $M(L) = \langle \rho \rangle L^3 \propto L^{3/(1-x)}$. Hence, the mass-scale power-law index $\gamma \equiv 3/(1-x)$ or:

$$x = \frac{\gamma - 3}{\gamma}. \quad (16)$$

Comparison between $x(2R_s)$ obtained in that way from the work of LAL10 and our model predictions $x(L)$ for sets (β, b, κ, T) is described in Paper I (see Fig. 1 there). The best fits $x(L)$ for the cloud complexes Taurus, Orion A and Orion B studied in this Paper are plotted in the left panels of Fig. 1, 2 and 3, respectively. We comment them in Section 3.

2.3 Derivation of the CIMF

A parameter set (β, b, κ, T) corresponding to the obtained best fit $x(L)$ of the LAL10 data for a chosen MC yields: i) a lognormal clump mass distribution $p_L(m)$; and ii) a measure of the total number of clumps $N_{\text{tot}}(L)$ at each scale (DVK11, Eq. 17):

$$N_{\text{tot}}(L) = \frac{1}{\kappa^3} \exp \left(\sigma^2 \times \frac{(x-1)(1-2x)}{2x^2} \right). \quad (17)$$

The CIMF of an individual cloud is derived as a superposition of the lognormal clump mass distributions. Each of them is discretized through sets of weights $\{N_L(m_j) = p_L(m_j)N_{\text{tot}}(L), j = 1, \dots, n\}$ where the mass range is centred at the peak of the distribution and the mass limits are determined from the requirement:

$$N_{\text{tot}}(L) = \sum_{j=1}^n N_L(m_j). \quad (18)$$

Also, to construct the CIMF correctly, one must require mass conservation throughout the MC fractal structure (Elmegreen 1997). The whole cloud with size equal to the upper limit of the inertial range $L_{\text{max}} = 20$ pc is to contain \mathcal{N}_L substructures of mass $M(L)$ at given scale L . As shown in Paper I (Sect. 3.2):

$$\mathcal{N}_L = \frac{L_{\text{max}}^{\frac{3}{1-x(L_{\text{max}})}}}{L^{\frac{3}{1-x(L)}}}. \quad (19)$$

Eventually, one obtains for the CIMF value in a selected mass bin $m' - \Delta m' \leq m \leq m' + \Delta m'$:

$$F_{\text{CIMF}}(m') = \sum_L \mathcal{N}_L \sum_m N_L(m). \quad (20)$$

If only gravitationally unstable clumps are considered, one should take also into account their contraction in timescales given by the free-fall time $\tau_{\text{ff}} \propto \rho^{-1/2}$. Their *time-weighted* mass function can be derived by permitting constant replenishment of the clump population and introducing a weighting factor of each scale of clump generation: $w(L, x(L)) \propto \tau_{\text{ff}}^{-1} \propto \langle \rho \rangle^{1/2} \propto L^{3x/2(1-x)}$ (cf. equations 2 and 11). Then the time-weighted CIMF is obtained as the number of substructures \mathcal{N}_L in equation 20 is modified by factor $w(L, x(L))/w(L_{\text{max}}, x(L_{\text{max}}))$.

3 RESULTS

We put to test the CIMF, derived in Paper I, using molecular line observations of nearby Galactic MC complexes and dust continuum studies of further 3 regions at kpc-scale distances, mapped also in CO lines (Table 1). Subsamples of the original clump data are considered taking into account the lower mass limit of confidence in our models and/or the observational completeness limit; the corresponding size and mass ranges are specified in columns 3 and 4.

3.1 Molecular line studies

Three individual nearby star-forming regions of comparable size are selected: i) with clumps delineated through similar density tracers: ^{13}CO (Orion B; Kramer et al. 1998), C^{18}O (Taurus; Onishi et al. 1996) and CS ($J = 1-0$) (Orion A; Tatematsu et al. 1993), consistent with the typical clump densities in our approach $n \sim 10^3 - 10^4 \text{ cm}^{-3}$; ii) with known general structure from dust extinction maps of LAL10. The spatial extent of the studied regions in the chosen complexes falls within the adopted inertial range of turbulence (Sect. 2.1, (i)). Dust extinction data reveal some diversity of structure in terms of mass-size relation of regions delineated by isodensity contours: Taurus exhibits monotonically 'steep' structure in terms of $x(L)$ while Orion A and Orion B have 'shallow' internal regions and 'steep' external, less dense regions (Fig. 1-3, left panels; cf. Fig. 2 in LAL10). Taurus is a typical low-mass star-forming region (Kenyon, Gómez & Whitney 2008), while numerous high-mass stars have been formed in Orion A and B in the recent past. As an additional test of the predictive power of the models for a variety of environments, we perform comparisons with observational CIMF for a sample of 9 MC complexes (Tachihara et al. 2002) wherein star-forming, cluster-forming and starless clumps have been detected.

An equipartition relation and a parameter set were sought that yield the best fit $x(L)$ of the cloud structure as traced by the LAL10 data (Fig. 1-3, left panels). The modeled CIMF derived from them is compared with the observational one from molecular line maps (Fig. 1-3, right

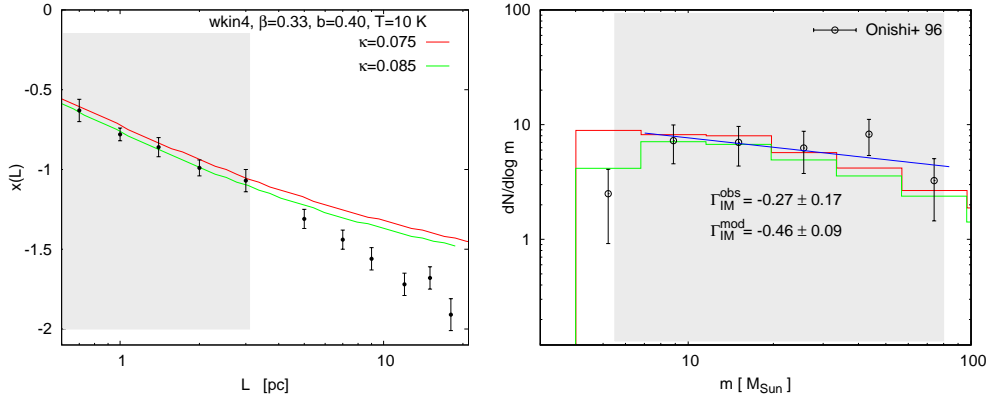


Figure 1. Structure and CIMF of the Taurus complex. *Left:* Best fits $x(L)$ of the data from LAL10 (dots with error bars) are plotted with lines and their characteristics (equipartition relation, model parameter values) are specified. *Right:* Clump mass functions, derived from the same models (lines), are juxtaposed with the observational CIMF from molecular line maps (open symbols with error bars). The range of scales of clump generation (left) corresponding to the observational clump mass range, restricted by the lower limit of confidence of the model (right) are shown with shaded areas. A weighted power-law fit of the observational CIMF (blue line) is drawn. Its slope (obs) and the one of the modeled intermediate-mass CIMF (mod) are specified.

Table 1. Observational clump samples used for comparison with the predictions of our model. Regions that are studied *both* by use of molecular line emissions and dust continuum data are put in bold. The slope estimates are re-derived by us, adopting mass limits corresponding to the applicability of our model and to the data completeness range. Notation: D = approximate distance to the region, IM = Intermediate-mass, HM = High-mass, γ^{obs} = Slope [$d \log m / d \log r$] on the clump mass-size diagram, M_{ch} = characteristic mass, CF = Clump-finding (method), PHM = contour at Half-Maximum around intensity peaks, PPV = Position-Velocity diagrams passing through intensity peaks; GB = gravitationally bound, UB = unbound

SF region	D [kpc]	Ref.	Sizes [pc]	Masses [M_{\odot}]	γ_{obs}	M_{ch} [M_{\odot}]	CIMF slope IM HM	CF method	Note
<i>Molecular line studies</i>									
Taurus	0.14	1	0.07 – 0.45	3 – 80	1.95	$\gtrsim 100$	–0.27 –	PHM	mostly GB
Orion A	0.45	2	0.06 – 0.35	30 – 1000	1.14	~ 300	–0.14 –1.82	PPV	$\sim 90\%$ starless, GB?
Orion B	0.45	3	0.06 – 0.70	3 – 200	1.95	~ 13	–0.17 –1.28	GAUSSCLUMPS	UB + GB
MC sample	≤ 0.18	4	0.08 – 0.45	3 – 60	2.09	~ 10	–0.25 –1.45	various	mainly starless, GB?
	≤ 0.18	4	0.08 – 0.45	3 – 100	2.09	~ 13	–0.44 –1.77	various	mainly starless, GB?
M 17	1.6	5	0.03 – 0.60	6 – 2300	1.77	$\gtrsim 200$	–0.34 –1.00	GAUSSCLUMPS	UB + GB?
Rosette	1.6	6	0.45 – 4.5	30 – 2000	2.40	$\gtrsim 800$	–0.28 –1.13	CLUMPFIND	starless, mostly UB?
<i>Dust continuum studies</i>									
M 17	1.6	7	0.02 – 0.70	1 – 600	2.13	$\sim 100?$	–0.35 –	CLUMPFIND	mainly starless
M 17 + NGC 7538		7, 8	0.06 – 0.60	3 – 1000	2.05	~ 100	–0.25 –1.82	CLUMPFIND	UB + GB?
Rosette	1.6	9	0.20 – 0.70	1.7 – 200	2.22	$\gtrsim 9$	–0.57 –1.04	GETSOURCES	starless

[1] Onishi et al. (1996); [2] Tatematsu et al. (1993); [3] Kramer et al. (1998); [4] Tachihara et al. (2002); [5] Stutzki & Güsten (1990); [6] Williams, Blitz & Stark (1995); [7] Reid & Wilson (2006a); [8] Reid & Wilson (2005); [9] Di Francesco et al. (2010)

panels). The range of spatial scales considered in the fitting procedure (shaded areas, left panels) corresponds to the mass range of the referred observational CIMF (shaded areas, right panels), additionally restricted by the lower clump mass limit of confidence in the model. The scales are treated as those where the observed clumps were generated and hence their range is obtained through the clump mass-scale diagram of the tested model (Paper I, Sect. 3.1).

3.1.1 Taurus

Fig. 1 (left) demonstrates that the equipartition choice **wkin4** yields a very good fit of the inner parts of the complex. That seems physically consistent to us since this case describes structures which have been shaped under significantly influence of self-gravity. The typical dense clumps generated in them have mass distributions in a relatively good agreement with the observational CIMF (Fig. 1, right), obtained by Onishi et al. (1996). The best-fit param-

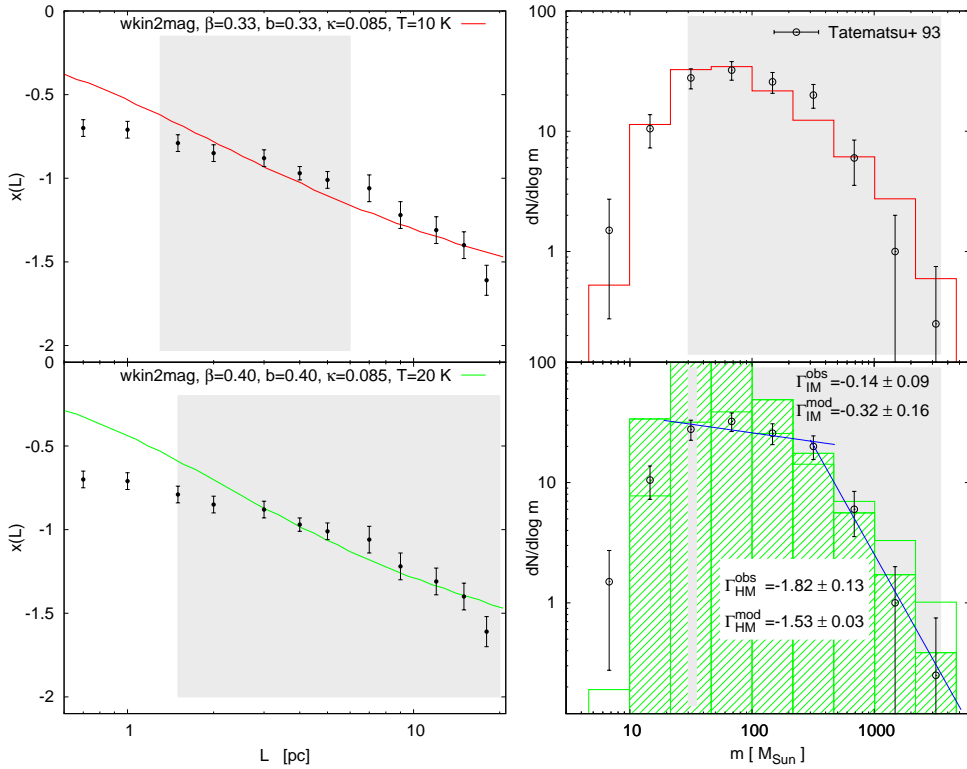


Figure 2. Structure and CIMF of the Orion A complex. The designations are the same like in Fig. 1; slopes of both intermediate-mass and high-mass CIMF are specified. The modeled non-time-weighted (lines) and time-weighted CIMFs (hatched area) are shown. The completeness limit of the observational data is adopted as a lower mass limit of confidence.

eters point to a mainly solenoidal turbulent forcing (see Federrath, Klessen & Schmidt 2008) and a ‘soft’ velocity scaling, typical for incompressible turbulence. On the other hand, the equipartition relation **wkin4** is obviously not applicable to the less dense extensive parts of the cloud. We stress, however, that in our model scales $L > 3$ pc do not produce clumps with masses within the considered observational range.

It should be pointed out that the CIMF obtained by Onishi et al. (1996) differs significantly from CIMFs in other clouds as derived from molecular line emission data. Using essentially the lowest mass bin ($\simeq 3 M_{\odot}$), these authors argue for a flat mass function¹ in Taurus, although they remain open for an alternative interpretation based on an “unbiased survey... in a wide mass range”. We believe that indeed their data cover the mass range around the turnover of the CIMF while its high-mass part (if existing) falls beyond their scope – note that characteristic masses M_{ch} of hundreds M_{\odot} are derived in various MC complexes (Table 1, column 7). The power-law slope of the modeled CIMF over the lower mass limit of confidence in our model is slightly shallower than the typical one of the mass distribution of CO clumps (Blitz 1993; Kramer et al. 1998). It would steepen ($\Gamma \sim -0.7$) if the observational data contained clumps with

masses up to the expected $M_{\text{ch}} \sim 200 M_{\odot}$ – cf. the modeled CIMFs from **wkin4** (Fig. 3 in Paper I).

3.1.2 Orion A

We obtained good fits of the Orion A structure in the case **wkin2mag** at intermediate to large spatial scales (Fig. 2, left). The corresponding CIMFs generally agree with the result of Tatematsu et al. (1993). Enhancement of the model temperature, compatible with the derived $T \sim 20$ K in the complex (Ikeda, Sunada & Kitamura 2007), leads to larger, more plausible values of b and β and yields a wider range of scales of clump generation as the cloud structure is better fitted through the curve $x(L)$ (Fig. 2, bottom).

Depending on the model temperature, the case **wkin2mag** in our approach generates mostly/only gravitationally unstable clumps (Paper I, Fig. 3). On the other hand, Tatematsu et al. (1993) claim that all clumps in their sample are close to virial equilibrium. Therefore a time-weighted CIMF (cf. Sect. 2.3) is more appropriate for comparison with the referred observational study. Time-weighting steepens the high-mass slope of the model from $\Gamma_{\text{HM}}^{\text{mod}} \sim -1$, typical for fractal clouds, to ~ -1.5 , i.e. steeper than that of the stellar IMF ($\Gamma \simeq -1.3$; Salpeter 1955) (Fig. 2, bottom right). This leads to agreement (within the data uncertainties) with the observational CIMF for clump masses $> M_{\text{ch}} \sim 300 M_{\odot}$ while for lower masses the devia-

¹ A shallow mass spectrum, in their terms.

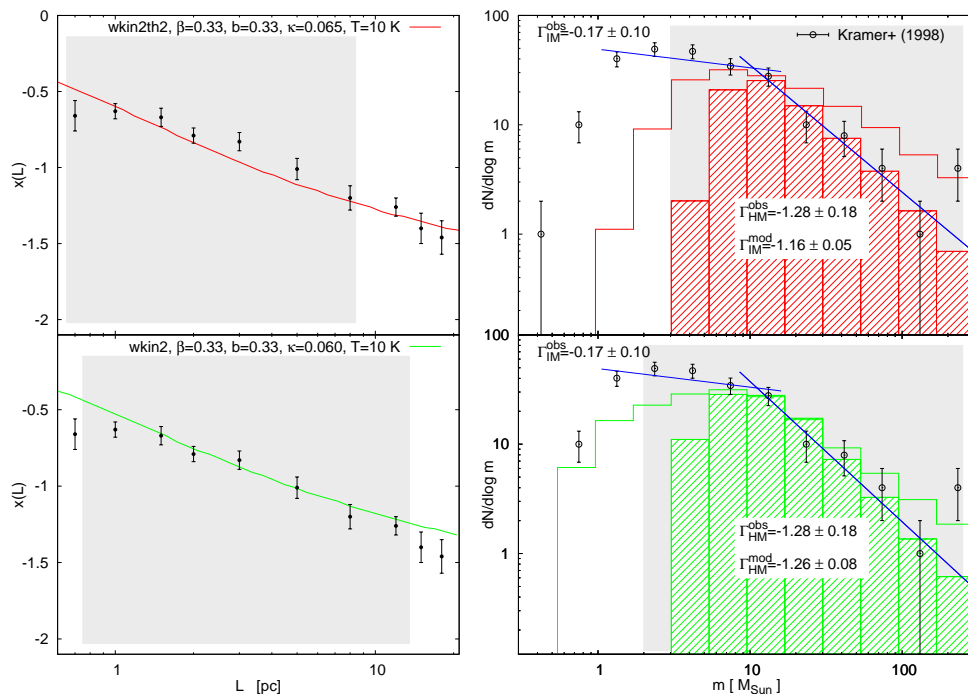


Figure 3. Structure and CIMF of the Orion B complex. The designations are the same like in Fig. 2.

tion is drastic. In contrast, the non-weighted modeled CIMF is generally consistent with the observational CIMF below M_{ch} and for $T = 20$ K. We note the high completeness limit ($\sim 30 M_{\odot}$) of the data which might artificially constrain the intermediate-mass range.

3.1.3 Orion B

The referred observational CIMF in this region is part of the work of Kramer et al. (1998) who analyzed CO data sets for 8 Galactic MCs. They argued for a single power-law CIMFs in all cases, with a universal mean slope $\Gamma \sim -0.7$, over a wide range of clump masses. However, a closer look at their result for Orion B reveals that this MC may be an exception. The conclusion of Kramer et al. (1998) about a single power-law with shallow slope is based mostly on the single mass bin $\gtrsim 200 M_{\odot}$ (Fig. 3, right). Inspection of the statistically rich data in the range $2 - 80 M_{\odot}$ indicate rather a combination of two power laws: a shallow intermediate-mass slope below $15 M_{\odot}$ and a significantly steeper high-mass slope. Adopting the latter value as M_{ch} and the completeness data limit of the authors $M \sim 1 M_{\odot}$, one obtains $\Gamma_{\text{IM}}^{\text{obs}}$ similar to that in Orion A and a Salpeter-like $\Gamma_{\text{HM}}^{\text{obs}}$.

Modeling of the Orion B structure as traced by the LAL10 data yields good fits in the cases **wkin2th2** and **wkin2** (Fig. 3, left). For such choices of equipartition and temperature $T = 10$ K, the critical mass over which most of the generated clumps are gravitational unstable is about the adopted characteristic mass from the used observational data. Therefore we apply time-weighting for the high-mass regime and obtain $\Gamma_{\text{HM}}^{\text{mod}}$ close to the Salpeter value. The

modeled CIMFs fit remarkably well the high-mass observational ones, excluding the sole bin at the upper limit of the distribution (Fig. 3, right). Non-weighted CIMFs obviously fail to reproduce the observational one although the high-mass slope ~ -0.7 is close to the estimate of Kramer et al. (1998). The model is not applicable to fit the intermediate-mass CIMF because of the high lower mass limit of confidence.

3.1.4 Sample of MC complexes

The presented best-fit descriptions $x(L)$ of MC structure in Taurus, Orion A and Orion B and their corresponding CIMFs with different characteristic masses M_{ch} and HM slopes (cf. Table 1) are derived by use of different equipartition relations that may reflect a variety of physical conditions. What model case would describe appropriately a statistical CIMF obtained from a large set of clump data in different MCs? The sample in the study of Tachihara et al. (2002) could give a clue to the answer – it encompasses nearby cloud complexes of diverse star-forming type as the vast majority of clumps are associated with no or a small number young stellar objects and have masses below several dozens M_{\odot} . Clumps associated with young stellar clusters were found in two out of nine sampled clouds and their fraction is only 5 % of the total number of clumps. All objects with masses $\geq 115 M_{\odot}$ are from this group. One may take the latter value as an upper mass limit when fitting the CIMF, in order to avoid extreme environments and to secure sufficient statistics. The two power-law shape of the CIMF is evident whereas the characteristic mass is ambiguous. We

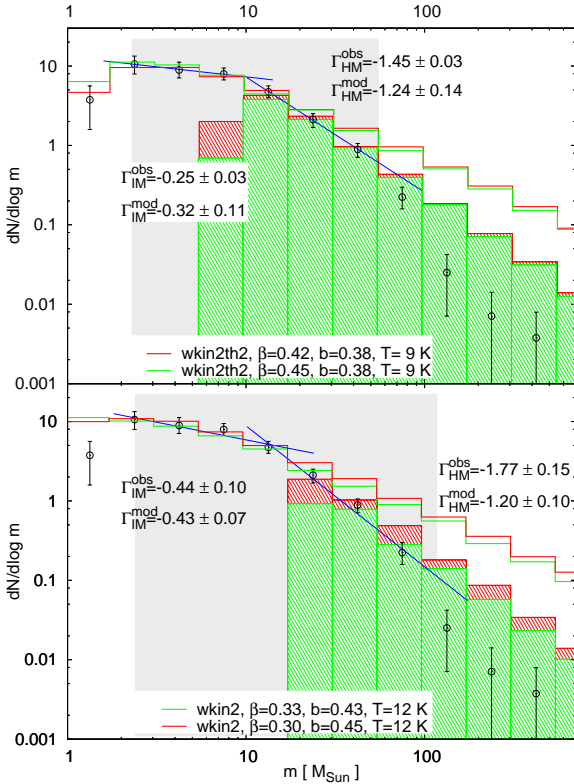


Figure 4. Modeling of the observational CIMF from 9 Galactic star-forming regions by use of the equipartition relations *wkin2* and *wkin2th2* for $\kappa = 0.065$ and adopting characteristic mass $\sim 10 M_{\odot}$ (top) and $\sim 13 M_{\odot}$ (bottom). See text for the considered mass ranges. Other designations are the same like in Figs. 1-3.

consider two choices which both allow for very good fits: i) $M_{\text{ch}} \sim 10 M_{\odot}$, adopting the estimate of Tachihara et al. (2002) and decreasing the upper mass limit further by one bin; and ii) $M_{\text{ch}} \sim 13 M_{\odot}$ (Fig. 4). The lower mass limit in both cases is the lower limit of confidence of the tested models.

The choice i) yields excellent agreement of the model case *wkin2th2* with the observational CIMF: time-weighted model for the HM part and non-time-weighted for the IM part (Fig. 4, top). The IM slope is very similar to the ones found in the considered individual MC complexes while the HM slope is about the Salpeter value, like in Orion B (Sect. 3.1.3). The discrepancy with the data for $m \gtrsim 60 M_{\odot}$ could be attributed to incompleteness of the sample in this mass range. A Salpeter-like slope is to be expected for mass distributions of (nearly) virialized clumps assuming their formation at a constant rate. The effect will be similar if the CIMF is derived from a statistically significant sample containing clumps in complexes at different evolutionary stages of clump formation. Note also that the variation of the velocity scaling index β in the fitting models is consistent with most observational and numerical works (e.g. Padoan et al. 2006, 2009). The values of the b param-

eter indicate preliminary solenoidal turbulent forcing with small contributions of the compressive mode.

Considering the choice ii), an upper mass limit $\sim 115 M_{\odot}$ is adopted as mentioned above. The model case *wkin2* provides an excellent fit of the intermediate-mass CIMF and a problematic one – for the high-mass CIMF. Again, the completeness of the clump mass bin $60 \leq m \leq 100 M_{\odot}$ is an open issue which is crucial for the correct slope estimation. On the other hand, the obtained low velocity scaling index β is consistent with results for Taurus, Orion A and Orion B.

Modeling of the observational CIMF from the equipartition cases *wkin2* and *wkin2th2* suggests that most of the clumps generated in MC complexes of diverse star-forming activity and with mean density about the typical local density (cf. Eq. 7 in Paper I) are in a state close to virial equilibrium.

3.1.5 Clump mass-size diagrams

An additional test for adequacy of the proposed statistical modeling of the CIMF is to construct clump mass-size diagrams. The comparison between the used observational data and the best-fit models of the observational CIMFs is displayed in Fig. 5. There are two difficulties with such analysis. First, the ‘average clump ensembles’ in our model occupy narrow strips on $m-r$ diagrams² whereas the dispersion of the observational samples is huge. Second, mass and (especially) size determinations from molecular-line maps depend essentially on the clump-finding technique which is different in each considered reference work (Table 1, column 10). A meaningful criterion is to compare the slope $\gamma^{\text{obs}} = (d \log m / d \log r)$ on the observational $m-r$ diagram with the predicted slopes γ^{mod} as the latter vary with the chosen equipartition case and the velocity scaling index β (cf. Paper I, Fig. C1).

The predicted slopes from the best-fit CIMF model are consistent with the ones from the referred molecular-line studies within 1σ limit for Taurus and Orion A and within about 2σ limit for Orion B and for the sample of Tachihara et al. (2002). In two cases, the ‘average clump ensemble’ strips cross the region of the observational data (Fig. 5, bottom). Taking into account the good agreement between observational and modeled CIMFs (Figs. 1-4), the shift between the two sets on the $m-r$ diagrams – with a factor of 2 toward larger (Orion A) or smaller sizes, – is to be interpreted with the variety of the clump size definition. The issue will be commented further in the next Section wherein we compare our model with CIMFs from dust continuum studies and in the Discussion.

3.2 Dust continuum studies

Sensitive submillimeter continuum maps are appropriate for probing the MC structure on small scales due to the optically thin dust emission. In the last decade, the achieved angular resolutions of $\lesssim 20''$ from ground-based observations (e.g. SCUBA, Bolocam) and space missions like HERSCHEL

² Clump sizes from our model are converted to radii $r = l/2$ to be compared with the radii of observed clumps.

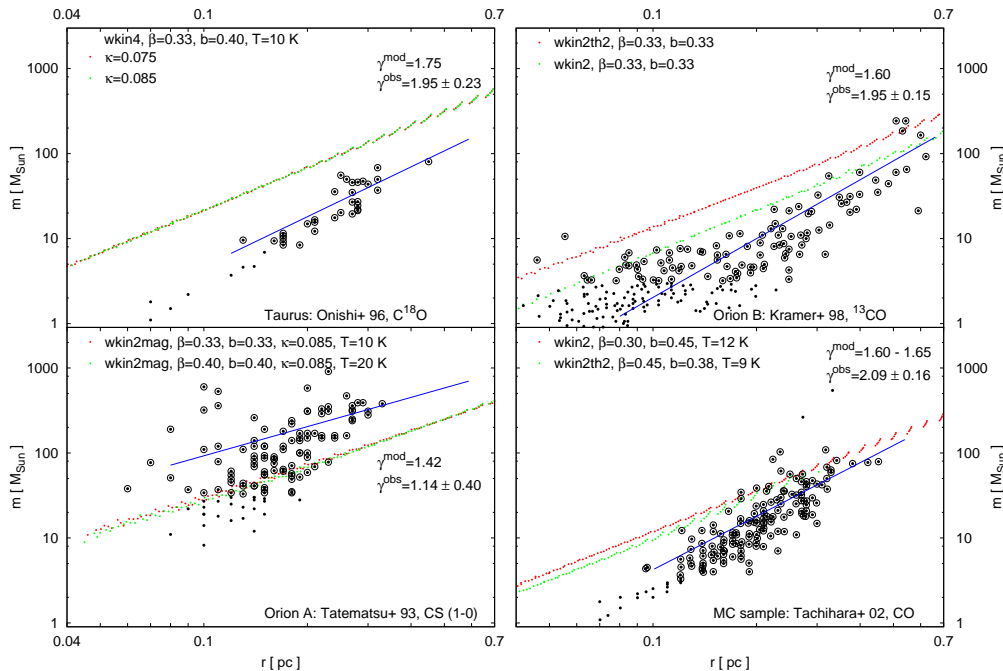


Figure 5. Clump mass-size diagrams from the referred molecular line studies. The data used to derive the CIMFs are shown with open symbols. The predictions of our model are plotted with dots, retaining the corresponding colors from Figs. 1-4.

allowed for study of clumps with sizes $\gtrsim 0.1$ pc in complexes at distances over 1 kpc. Therefore it is instructive to compare results from such studies with our model. In view of the complexes' remoteness, the considered regions were not included in the work of LAL10 and we don't have at our disposal their dust extinction mapping as a tool to trace and fit the general cloud structure (cf. Figs. 1-3, left). To compensate this lack, we chose star-forming regions which clump population has been probed also by use of molecular-line maps. The observational CIMF was fitted directly and the clump mass-size diagram was used as an additional test.

3.2.1 M17

Large part of this massive star-forming region was mapped by Reid & Wilson (2006a) in two SCUBA bands. We use here the clump data from their $850 \mu\text{m}$ map because of the richer statistics. The fitting of the observational CIMF and the corresponding clump-mass size diagram are plotted in Fig. 6 (top). A very good fit of the CIMF is achieved from the model case **wkin4** that points to strongly gravitationally bound clumps. The predicted and the observational clump mass-size diagrams are also in agreement (Fig. 6, right top). Note that we assumed a higher gas temperature $T = 20$ K which is about the average clump temperature derived by the authors.

Although Reid & Wilson (2006a) suggest a two power-law CIMF with $M_{\text{ch}} \sim 8 M_{\odot}$, it seems that their result hints rather at an order-of-magnitude higher characteristic mass. This is supported by the slope in the mass range $10 \lesssim m \lesssim 100 M_{\odot}$ which is similar to the IM slopes found

from the referred molecular-line studies (cf. Table 1). However, only two clumps with masses $> 100 M_{\odot}$ in the observational sample are far from sufficient for a plausible estimate of the characteristic mass. To clarify the issue, we apply our method to a C^{18}O study of the south-western sector of M17 (Stutzki & Güsten 1990). As demonstrated in Fig. 6, bottom, the results for an intermediate-mass CIMF with $M_{\text{ch}} \sim 100 M_{\odot}$ are virtually the same, fitted from the same model case and free parameter values and slightly higher temperature. Moreover, the high-mass CIMF is also well fitted by the time-weighted mass distribution of gravitationally unstable clumps. Neglecting the mass bin $> 2000 M_{\odot}$, which contains only 2 clumps, the slope Γ_{HM} is shallower than that of the stellar IMF.

For independent confirmation of this result, we composed a twice larger sample, including clump data from a similar study of NGC 7538 (Reid & Wilson 2005). As shown in Fig. 7, the CIMF is fitted again from the model case **wkin4** and a similar parameter set (β, b) for a large range of clump masses $7 \lesssim m \lesssim 1000 M_{\odot}$, applying time-weighting for the more massive clumps. In comparison to the mass distribution from the M17 sample, the IM slope shallows slightly and approaches the values from the molecular-line studies of nearby MC complexes (cf. Table 1) while the HM slope is much steeper than that from Stutzki & Güsten's study and is identical with the one in Orion A (Fig. 2) although with a smaller M_{ch} . The agreement of the model with the clump data on the $m-r$ diagram is again excellent (Fig. 7, right).

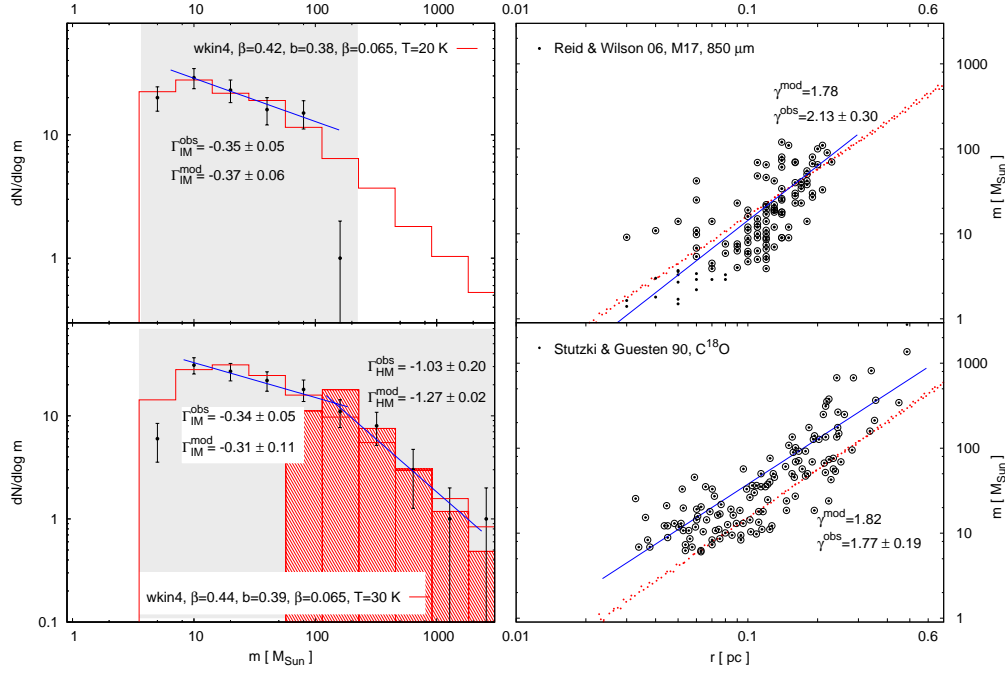


Figure 6. CIMF and clump mass-size diagrams of the star-forming region M17 from dust-continuum (top) and molecular-line (bottom) observations. The shaded areas denote the observational mass range restrained by the lower-mass confidence limit from the model – the corresponding data used to derive the CIMFs are shown with open symbols in the M-R diagram. The predictions of the model are plotted with the same colors in the left (lines) and right (dots) panels.

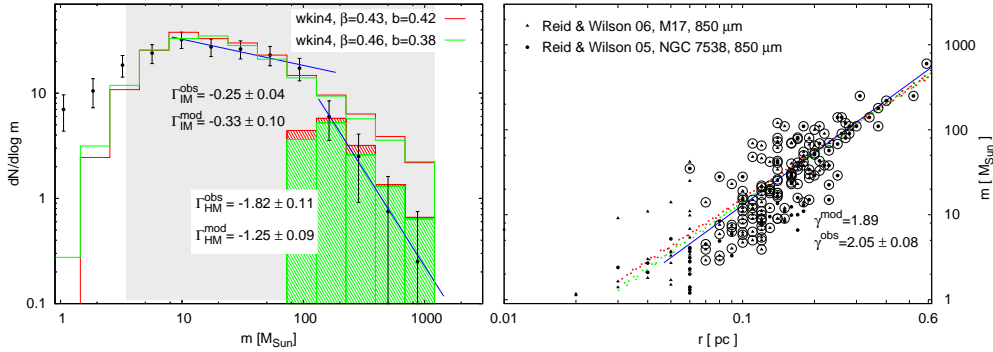


Figure 7. Combined CIMF and clump mass-size diagram of the star-forming regions M17 and NGC 7538 from dust-continuum observations. The designations are the same like in Fig. 6. The values of $\kappa = 0.065$ and $T = 30$ K are retained without change from the fitting of the M17 sample only.

3.2.2 Rosette molecular cloud

The abundant observational studies of this complex in the outer Galaxy indicated active star formation in the past and nowadays. Its clump population has been studied both on molecular-line and dust continuum maps; we chose the works of Williams, Blitz & Stark (1995) and Di Francesco et al. (2010), respectively. The high-quality HERSCHEL data used by the latter authors allow for derivation of the CIMF in a mass range spanning three orders of magnitude (Fig.

8, top left). Some incompleteness is sensible in the mass bins $\gtrsim 10 M_{\odot}$ and has – in our view, – two possible explanations. First, for the sake of our study we selected only starless clumps from the original sample. Second, Di Francesco et al. (2010) applied the GETSOURCES algorithm (Men'shchikov et al. 2012) for clump decomposition which favors identification of more compact (and less massive) objects.

Because of the lower mass-limit of confidence, our statistical method is not able to fit the CIMF below $\sim 2 M_{\odot}$.

The observed mass distribution for larger masses could be interpreted as single power-law CIMF with a slope about -1 (not shown). In view of the possible incompleteness of the high-mass clump data, we suggest rather a two power-law mass function, fitted from the model case **wkin2** (Fig. 8, top left). The characteristic mass for **wkin2** and for the obtained best-fit parameters is $\sim 9 M_\odot$ (see Fig. 3 in Paper I). Adopting this value for M_{ch} , one gets a bit steeper intermediate-mass CIMF than found for other MC complexes in this Paper and a high-mass CIMF, with a slope typical for fractal clouds (Elmegreen 1997). On the clump mass-size diagram, a shift of the model from the observed clumps is evident like in some other studied regions: by a factor of 2 to 4 (Fig. 8, top right; cf. Fig. 5). Nicola Schneider (private communication) provided for us estimates of the cloud mass M as a function of spatial scale L , calculated from the original *HERSCHEL* column density map of Rosette. That enabled a check of the derived best-fit model with the observed cloud structure, in terms of the LAL10 work (Figs. 1-3, left). The shape of the modeled curve $x(L)$ is consistent with the dust-continuum data but with a shift toward lower x . Decreasing the mapping resolution parameter down to $\kappa = 0.02$, we found excellent agreement with the data (Fig. 8, right, embedded diagram). That is illustrative how the observed general cloud structure affects the κ -parameter space of the CIMF fitting.

Williams, Blitz & Stark (1995) derived the observational CIMF from CO mapping of Rosette MC. As seen in Fig. 8 (bottom), their clump size range practically does not overlap with the one of Di Francesco et al. (2010) while the mass range spans from 10 to $> 1000 M_\odot$. The CIMF is well fitted from the model case **wkin2mag** and a very ‘soft’ velocity scaling, $\beta \simeq 0.20$. Such values of the scaling index were found from magneto-hydrodynamic simulations of Collins et al. (2012).

4 DISCUSSION

The comparison with the considered molecular-line and dust-continuum studies of Galactic MC complexes demonstrates the applicability of a statistical approach to derive the CIMF presented in Paper I. The results on fitting the observational CIMF through our model are summarized in Table 2. They are obtained by use of two different primary fitting criteria: fitting of the general cloud structure $x(L) - L$ or direct fitting of the CIMF. Regardless of the type of observational data, the applied fitting criterion and of the variety of model cases, the best-fit parameters span relatively narrow ranges:

- ‘Soft’ velocity scaling: $0.20 \lesssim \beta \lesssim 0.46$
- Mainly solenoidal forcing: $0.30 \leq b \leq 0.46$
- Mapping resolution from few percent to one tenth of the spatial scale: $0.02 \leq \kappa \leq 0.10$
- Typical temperatures for molecular gas phase: $8 \leq T \leq 35$ K.

A small velocity scaling index β , close or equal to the Kolmogorov value for incompressible turbulence (0.33), may seem unrealistic in view of the high compressibility of interstellar turbulence which implies $\beta \sim 0.50$. In fact, numerical simulations of magnetized clouds show that the

velocity power spectrum can be even shallower than in the Kolmogorov theory. Collins et al. (2012) measured $\beta = 0.23 - 0.29$ for thermal-to-magnetic pressure ratio in range $0.2 - 2.0$. (In our modeling, the latter value could be as low as $\simeq 0.05$ in case **wkin2mag**; see Eq. 3.) Apparently, the velocity scaling index for incompressible turbulence $\beta = 0.33$ should not be necessarily treated as the lowest possible value from theoretical considerations.

The best-fit range of the turbulent forcing parameter b is narrower, with typical values $0.38 - 0.40$, in most considered complexes. Since b can vary within a star-forming region, this result might be explained as a statistical effect. Indeed, $b \simeq 0.40$ corresponds to a natural mixture between solenoidal and compressive modes as the latter represent longitudinal waves, occupying one of the three spatial dimensions (see Federrath et al. 2010, and Fig. 8 there). The typical best-fit values of the mapping resolution parameter κ are about several percent. These are the expected values, appropriate to distinguish substructures which are significantly smaller than the spatial scale L and significantly larger than the scale of dissipation.

Generally, our results lend support to a two power-law shape of the CIMF: intermediate-mass and high-mass part, with two distinct values of the characteristic mass M_{ch} : ~ 10 and $\sim 200 M_\odot$. (The molecular-line study of Rosette MC with its high M_{ch} is the only exception.) The first value is consistent with model cases of a ‘virial-like’ equipartition between gravitational and turbulent energy, possibly with contribution of the thermal energy at small scales and negligible contribution of the magnetic energy (**wkin2**, **wkin2th2**). These equipartition relations are not sufficient to argue that the modeled clumps are in virial equilibrium (Ballesteros-Paredes 2006) but rather indicate their gravitational boundedness or contraction. On the other hand, if the considered model cases hold for a whole cloud, they are indicative for its global collapse (Vázquez-Semadeni et al. 2007). Large characteristic masses of hundreds M_\odot are obtained for strongly gravitating clumps, with possible magnetic support (**wkin4**, **wkin2mag**). Such are evidently the cases in Taurus, Orion A, M 17 and NGC 7538.

The slope of the modeled intermediate-mass CIMF is shallow and does not vary significantly from complex to complex ($-0.26 \geq \Gamma_{\text{IM}}^{\text{mod}} \geq -0.56$) while the variety is larger for the high-mass one: from typical slopes for fractal clouds to slopes, a bit steeper than the one of the stellar IMF ($-0.9 \gtrsim \Gamma_{\text{HM}}^{\text{mod}} \gtrsim -1.5$). It seems that the single power-law observational CIMFs of slope $-0.7 \gtrsim \Gamma^{\text{obs}} \gtrsim -0.8$ derived from molecular-line studies in 1990s (Stutzki & Güsten 1990; Blitz 1993; Heithausen et al. 1998) have been products of a combination between intermediate- and a few bins from high-mass CIMF. On the other hand, the variety of high-mass CIMF slopes probably reflects a real variety of physical conditions in individual complexes and the gravitational balance and evolution of the dense fragments in them. Its model slope $\Gamma_{\text{HM}}^{\text{mod}}$ similar to that of the stellar IMF when the CIMF is time-weighted. When derived from molecular-line mapping of Orion A (Tatematsu et al. 1993) or the dust-continuum studies of M 17 and NGC 7538 by Reid & Wilson (2005, 2006a), $\Gamma_{\text{HM}}^{\text{obs}}$ exceeds noticeably the Salpeter value but lies still within the observed variability range (Kroupa 2001).

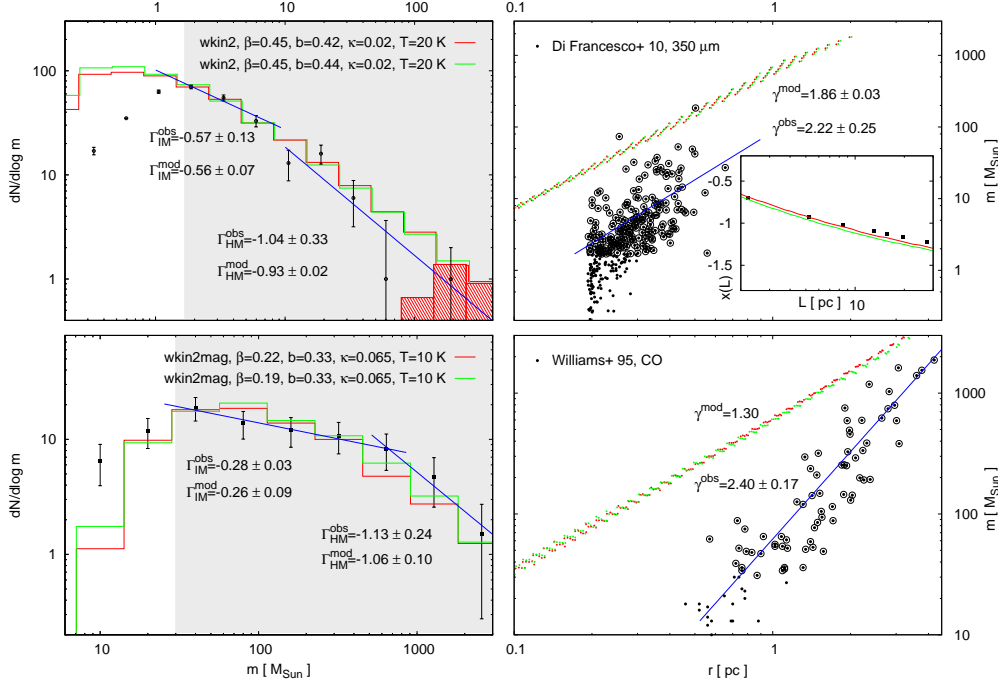


Figure 8. CIMF and clump mass-size diagrams of the Rosette MC from dust-continuum (top) and molecular-line (bottom) observations. The designations are the same like in Fig. 6. A comparison between the predictions of the illustrated models and the observed structure from a column density map using Herschel FIR-continuum data (N. Schneider, priv. comm.) is embedded in the top-right panel.

The dust extinction mapping of Taurus, Orion A and Orion B by LAL10 enabled us to make a link between the predicted general cloud structure and the CIMF. We point out also the excellent agreement applying this criterion to the dust-continuum study of Rosette, making use of a column density map of Rosette (Fig. 8, top right, embedded) obtained from HERSCHEL DATA (see Schneider et al. 2012, for details). (Note that the extinction map derived from near-IR extinction using 2MASS (Schneider et al. 2011) delivers similar values for $A_V \lesssim 10^m$.) Generally, good agreement is found for the chosen scales of clump generation L between ~ 0.5 and ~ 15 pc while in Taurus the upper limit is about half of that. Those are the conservative limits of the inertial range of turbulence³ that is a cornerstone in our framework of clump description. The discrepancies for larger L are to be expected and can be interpreted as reflecting changes in the physical conditions – such scales may lie outside the inertial range and/or the assumption of isothermality does not hold for them (e.g. Hennebelle et al. 2008). On the other hand, at $L \lesssim 1$ pc the density PDF deviates from the lognormal shape and develops a power law tail in the high-density part (Klessen 2000; Kritsuk, Norman & Wagner 2011). The predicted typical clump size in such density regimes approaches ~ 0.1 pc which is about the sonic scale for temperature range 10 – 20 K, i.e. the assumption for supersonic turbulence as a generator of clumps breaks down.

Inclusion of data from dust-continuum studies in the analysis of the clump mass-size ($m - r$) diagrams confirms the results from molecular-line mappings (Sect. 3.1.5): consistency between the slopes within 2σ and, occasionally, a shift by a factor of up to 3 on the size axis. Generally, the agreement between the locations of the ‘average clump ensemble’ and the observed clumps is better; especially, for the combined clump sample from M 17 and NGC 7538. The discrepancies on the $m - r$ diagrams could be attributed to the various clump-finding techniques used in the referred observational studies (cf. Table 1, column 10) and hence to different clump size definitions. The latter would not lead to substantially different mass estimates if a typical clump structure is a dense central region and diffuse outer shell. A careful comparative analysis of the basic clump-finding algorithms, applied to identical observational or numerical datasets, is necessary for a more comparison between our statistical clump description and the observed clumps in MC complexes.

The role of the magnetic fields in shaping the physical characteristics of MCs and of their substructures can be accounted for more thoroughly in a further extension of this work. Molina et al. (2012) proposed an analytical model of the relation between the width of the PDF σ in magnetized turbulent medium. It includes a modification of equation 5, consistent with a scaling law of magnetic field $B \propto \langle \rho \rangle^{1/2}$ (equation 3) and can be easily incorporated in our modeling.

Finally we caution the reader that the predictions of our model hold for less evolved clumps of sizes $\gtrsim 0.1 - 0.2$ pc and must not be compared with observational mass distri-

³ We recall here the comment in Sect. 2.1, i)

Table 2. Summary of the results on fitting the observational CIMF in the considered molecular cloud complexes. The probed parameter ranges (below the table) and the ranges of the model parameters that give good fits (Columns 3-7) are specified. Notation: FC = Fitting Criterion ($x - L$ – general cloud structure on $x(L) - L$ diagram; CIMF – direct fitting of the CIMF), MC = model case.

SF region	FC	MC	Model parameter ranges				CIMF				$m-r$ slope	
			β	b	κ	T [K]	$\Gamma_{\text{IM}}^{\text{obs}}$	$\Gamma_{\text{IM}}^{\text{mod}}$	$\Gamma_{\text{HM}}^{\text{obs}}$	$\Gamma_{\text{HM}}^{\text{mod}}$	$\gamma_{\text{obs}}^{\text{obs}}$	$\gamma_{\text{mod}}^{\text{mod}}$
Molecular line studies												
Taurus	$x-L$	wkin4	0.30-0.36	0.38-0.42	0.07-0.09	10-20	-0.27 ± 0.17	-0.46 ± 0.09	–	–	1.95 ± 0.23	1.75
Orion A	$x-L$	wkin2mag	0.38-0.42	0.38-0.42	0.07-0.09	18-22	-0.14 ± 0.09	-0.32 ± 0.16	-1.82 ± 0.13	-1.53 ± 0.03	1.14 ± 0.40	1.42
Orion B	$x-L$	wkin2	0.30-0.36	0.30-0.36	0.055-0.065	10-15	-0.17 ± 0.10	–	-1.28 ± 0.18	-1.26 ± 0.08	1.95 ± 0.15	1.62
MC sample	$x-L$	wkin2th2	0.30-0.36	0.30-0.36	0.050-0.065	10-15	-0.17 ± 0.10	–	-1.28 ± 0.18	-1.16 ± 0.05	1.95 ± 0.15	1.60
	CIMF	wkin2	0.30-0.36	0.42-0.46	0.02-0.10	10-12	-0.44 ± 0.10	-0.43 ± 0.07	-1.77 ± 0.15	-1.20 ± 0.10	2.09 ± 0.16	1.60
	CIMF	wkin2th2	0.42-0.46	0.36-0.40	0.02-0.10	8-10	-0.25 ± 0.03	-0.32 ± 0.11	-1.45 ± 0.03	-1.24 ± 0.14	2.09 ± 0.16	1.65
M 17	CIMF	wkin4	0.43-0.45	0.37-0.40	0.02-0.10	28-35	-0.34 ± 0.05	-0.31 ± 0.11	-1.03 ± 0.20	-1.27 ± 0.02	1.77 ± 0.19	1.82
Rosette	CIMF	wkin2mag	0.18-0.23	0.30-0.36	0.02-0.10	8-15	-0.28 ± 0.03	-0.26 ± 0.09	-1.13 ± 0.24	-1.06 ± 0.10	2.40 ± 0.17	1.30
Dust continuum studies												
M 17	CIMF	wkin4	0.40-0.44	0.37-0.40	0.02-0.10	28-35	-0.35 ± 0.05	-0.37 ± 0.06	–	–	2.13 ± 0.30	1.78
M 17+	CIMF	wkin4	0.43-0.46	0.38-0.42	0.02-0.10	28-35	-0.25 ± 0.04	-0.33 ± 0.10	-1.82 ± 0.11	-1.25 ± 0.09	2.05 ± 0.08	1.89
Rosette	CIMF	wkin2	0.44-0.46	0.41-0.45	0.02-0.03	18-25	-0.57 ± 0.13	-0.56 ± 0.07	-1.04 ± 0.33	-0.93 ± 0.02	2.22 ± 0.25	1.86
	$(x-L)$											

Probed parameter spaces: $0.18 \leq \beta \leq 0.65$; $0.30 \leq b \leq 0.55$; $0.02 \leq \kappa \leq 0.10$; $8 \leq T \leq 40$ K

butions of dense (prestellar) cores. The latter ones will be subject of another study which considers the high-density power-law tail of the density PDF (cf. Kainulainen et al. 2009; Kritsuk, Norman & Wagner 2011) in active star forming regions as a basis for cores' description. The essence of this approach is presented in Donkov, Stanchev & Velchev (2012) while the model is in process of development. Such study may answer the question whether the difference between the clump mass function and the core mass function is physical or statistical.

5 SUMMARY

Our statistical approach for physical description of condensations (clumps) formed through a turbulent cascade during the early MC evolution predicts: i) the cloud structure in terms of effective size-mass scaling relations, through the mass-density exponent x as a function of the spatial scale L (DVK11); and ii) the composite clump mass function (CIMF; Paper I). Different models within this framework are generated by choosing an appropriate energy equipartition relation and a set of 4 free parameters: velocity scaling index β , turbulent forcing parameter b , mapping resolution parameter κ and temperature T . In this Paper we compared CIMFs from molecular-line and dust-continuum studies of Galactic cloud complexes with ones derived from our model applying alternative fitting criteria: fitting the structure $x(L)$ of individual complexes (when additional dust-extinction data are available) or direct fitting of the observational CIMF.

Both fitting criteria lead to modeled clump mass distributions, in good or excellent agreement with the considered observational data. The equipartition relations which yield these fits indicate gravitational boundedness of the dominant clump population in the considered clouds, possibly including the contribution of magnetic or thermal energy:

model cases **wkin2**, **wkin2th2** or **wkin2mag**. On the other hand, the results for Taurus, M17 and NGC 7538 rather hint at strongly gravitating or contracting inner parts of those complexes (model case **wkin4**). The derived best-fit values of the parameters β , b and T for all studied individual clouds span relatively narrow ranges. In most MC complexes the typical velocity scaling index is found to be similar to the original ‘‘Larson’s first law’’ (Eq. 1, $\beta = 0.38$) or to $\beta \sim 0.43$ testified from recent observations (Padoan et al. 2006, 2009). The best-fit values of the turbulent forcing parameter concentrate around $b \simeq 0.40$ which corresponds to a natural mixture between compressive and solenoidal modes (Federrath et al. 2010).

The modeled clump mass distributions support a CIMF which might be represented as a combination of two-power law functions. The latter are separated by a characteristic mass M_{ch} that varies typically within one order of magnitude or more: from about ten to hundreds solar masses. The slope of the intermediate-mass CIMF is shallow and nearly constant: $-0.25 \gtrsim \Gamma_{\text{IM}} \gtrsim -0.55$. The high-mass part of the CIMF corresponds to gravitationally unstable clumps in all considered model cases and hence a more appropriate description should take into account the dynamical clump evolution. Such description is achieved through time-weighting of the clump mass distribution. (The effect will be similar if the CIMF is derived from a statistically significant sample containing clumps in MC complexes at different evolutionary stages of clump formation.) We obtained slopes within a broader range $-0.9 \gtrsim \Gamma_{\text{HM}} \gtrsim -1.6$ that includes the typical value for fractal clouds -1 (Elmegreen 1997) as well that of the stellar initial mass function (Salpeter 1955).

Comparison between the observational and the modeled clump mass-size diagrams reveals agreement of the slopes within the 2σ limit and, in most cases, a systematic shift toward smaller or larger clump sizes. The latter is to be

attributed to variety of size definitions used in the different clump-finding techniques.

Acknowledgement: We are grateful to the anonymous referee for his/her insightful comments and recommendations which helped us to improve substantially this Paper. We thank J. Di Francesco for the list of clump properties in Rosette MC derived from HERSCHEL data, and N. Schneider for providing us the mass/spatial scale values shown in Fig. 8 from the same Herschel column density map. We appreciate the help of V. Ossenkopf and R. Simon who provided for us data on the individual clump characteristics in Orion B from the original study of Kramer et al. (1998).

T.V. acknowledges support by the *Deutsche Forschungsgemeinschaft* (DFG) under grant KL 1358/15-1.

REFERENCES

- Alves, J., Lombardi, M., Lada, C., 2007, *A&A*, 462, L17
- Ballesteros-Paredes, J., & Vázquez-Semadeni, E., 1995, *RevMexAA*, Ser. Conf., 3, 105
- Ballesteros-Paredes, J., 2006, *MNRAS*, 372, 443
- Banerjee, R., Vázquez-Semadeni, E., Hennebelle, P., Klessen, R. S., 2009, *MNRAS*, 398, 1082
- Bergin, E., Tafalla, M., 2007, *ARA&A*, 45, 339
- Blitz, L., 1993, in: Levy, E., Lunine, J., eds., *Protostars and Planets III*. The University of Arizona Press, Tuscon & London
- Collins, D., Kritsuk, A., Padoan, P., Li, H., Xu, H., Ustyugov, S., Norman, M., 2012, *ApJ*, 750, 13
- Crutcher, R., 1999, *ApJ*, 520, 706
- Di Francesco, J., Sadavoy, S., Motte, F., Schneider, N., Hennemann, M., Csengeri, T., Bontemps, S., Balog, Z., et al., 2010, *A&A*, 518, L91
- Donkov, S., Stanchev, O., Veltchev, T., 2012, *Proc. of the VIII Serbian-Bulgarian Astron. Conf.*, Leskovac, Serbia, May 8-12, 2012, eds. M. K. Tsvetkov, M. S. Dimitrijevic, K. Tsvetkova, O. Kounchev, Z. Mijajlovic (arXiv 1206.1444)
- Donkov, S., Veltchev, T., Klessen, R. S., 2011, *MNRAS*, 418, 916 (DVK11)
- Donkov, S., Veltchev, T., Klessen, R. S., 2012, *MNRAS*, 423, 889 (Paper I)
- Elmegreen, B. G., 1997, *ApJ*, 486, 944
- Enoch, M., Evans, N., Sargent, A., Glenn, J., Rosolowsky, E., Myers, P., 2008, *ApJ*, 684, 1240
- Federrath, C., Klessen, R., Schmidt, W., 2008, *ApJ*, 688, L79
- Federrath, C., Roman-Duval, J., Klessen, R., Schmidt, W., Mac Low, M.-M., 2010, *A&A*, 512, 81
- Hara, A., Tachihara, K., Mizuno, A., Onishi, T., Kawamura, A., Obayashi, A., Fukui, Y., 1999, *PASJ*, 51, 895
- Heithausen, A., Bensch, F., Stutzki, J., Falgarone, E., Panis, J., 1998, *A&A*, 331L, 65
- Hennebelle, P., Banerjee, R., Vázquez-Semadeni, E., Klessen, R. S., Audit, E., 2008, *A&A*, 486, L43
- Ikeda, N., Sunada, K., Kitamura, Y., 2007, *ApJ*, 665, 1194
- Ikeda, N., Kitamura, Y., Sunada, K., 2009, *ApJ*, 691, 1560
- Johnstone, D., Fich, M., Mitchell, G., Moriarty-Schieven, G., 2001, *ApJ*, 559, 307
- Johnstone, D., Matthews, H., Mitchell, G., 2006, *ApJ*, 639, 259
- Kainulainen, J., Beuther, H., Henning, T., Plume, R., 2009, *A&A*, 508, L35
- Kenyon, S., Gómez, M., Whitney, B., 2008, in *Handbook of Star Forming Regions*, Vol. I, ed. B. Reipurth (San Francisco, CA: ASP), 405
- Kerton, C., Martin, P., Johnstone, D., Ballantyne, D., 2001, *ApJ*, 552, 601
- Klessen, R. S., 2000, *ApJ*, 535, 869
- Klessen, R. S., & Hennebelle, P., 2010, *A&A*, 520, A17
- Könyves, V., André, P., Men'shchikov, A., Schneider, N., Arzoumanian, D., Bontemps, S., Attard, M., Motte, F., et al., 2010, *A&A*, 518, L106
- Kramer, C., Stutzki, J., Rohrig, R., Corneliussen, U., 1998, *A&A*, 329, 249
- Kritsuk, A., Norman, M., Padoan, P., & Wagner, R., 2007, *ApJ*, 665, 416
- Kritsuk, A., Norman, M., & Wagner, R., 2011, *ApJ*, 727, L20
- Kroupa, P., 2001, *MNRAS*, 322, 231
- Larson, R., 1981, *MNRAS*, 194, 809
- Lombardi, M., Alves, J., Lada, C., 2010, *A&A*, 519, 7 (LAL10)
- Men'shchikov, A., André, P., Didelon, P., Motte, F., Hennemann, M., Schneider, N., 2012, *A&A*, 542, 81
- Molina, F., Glover, S., Federrath, C., Klessen, R., 2012, *MNRAS*, 423, 2680
- Motte, F., André, P., Neri, R., 1998, *A&A*, 336, 150
- Motte, F., André, P., 2001, *ASP Conf. Series*, vol. 243, eds. T. Montmerle & P. André, 301
- Nutter, D., Ward-Thompson, D., 2007, *MNRAS*, 374, 1413
- Onishi, T., Mizuno, A., Kawamura, A., Ogawa, H., Fukui, Y., 1996, *ApJ*, 465, 815
- Onishi, T., Mizuno, A., Kawamura, A., Tachihara, K., Fukui, Y., 2002, *ApJ*, 575, 950
- Padoan, P., Juvela, M., Kritsuk, A., Norman, M., 2006, *ApJ*, 653, L125
- Padoan, P., Juvela, M., Kritsuk, A., Norman, M., 2009, *ApJ*, 707, L153
- Passot, T., Vázquez-Semadeni, E., & Pouquet, A., 1995, *ApJ*, 455, 536
- Reid, M., Wilson, C., 2005, *ApJ*, 625, 891
- Reid, M., Wilson, C., 2006, *ApJ*, 644, 990
- Reid, M., Wilson, C., 2006, *ApJ*, 650, 970
- Salpeter, E., 1955, *ApJ*, 121, 161
- Schneider, N., Bontemps, S., Simon, R., Ossenkopf, V., Federrath, C., Klessen, R. S., Motte, F., André, Ph., 2011, *A&A*, 529, 1
- Schneider, N., Csengeri, T., Hennemann, M., Motte, F., Didelon, P., Federrath, C., Bontemps, S., Di Francesco, J., et al., 2012, *A&A*, 540, 11
- Shetty, R., Collins, D., Kauffmann, J., Goodman, A., Rosolowsky, E., & Norman, M., 2010, *ApJ*, 712, 1049
- Stanke, T., Smith, M., Gredel, R., Khanzadyan, T., 2006, *A&A*, 447, 609
- Stutzki, J., & Güsten, R., 1990, *ApJ*, 356, 513
- Tachihara, K., Mizuno, A., Fukui, Y., 2000, *ApJ*, 528, 817
- Tachihara, K., Onishi, T., Mizuno, A., Fukui, Y., 2002, *A&A*, 385, 909
- Tatematsu, K., Umemoto, T., Kameya, O., et al., 1993, *ApJ*, 404, 643
- Testi, L., Sargent, A., 1998, *ApJ*, 508, L91
- Vázquez-Semadeni, E., Gómez, G., Jappsen, A.,

- Ballesteros-Paredes, J., González, R., Klessen, R.
S., 2007, ApJ, 657, 870
Williams, J., Blitz, L., Stark, A., 1995, ApJ, 451, 252